RSC Advances

PAPER

View Article Online
View Journal | View Issue

Cite this: *RSC Adv.*, 2020, **10**, 34387

The role of alloyed strontium in the microstructures and alkaline electrochemistry of Mg–5Al–4Sn alloys

Le Van Sy,[a] Phan Minh Quoc Binh,[a] Bhajan Lal,[b] Quy Bau Nguyen,[c] Tran Van Hung,*[de] Casen Panaitescu*[f] and Nguyen Dang Nam *[de]

In this study, strontium is used as an alloying element for improving the pitting resistance of Mg–5Al–4Sn based alloys in an alkaline solution. Potentiodynamic polarization measurements suggest that the addition of strontium increases the robustness of the pitting resistance as a result of the higher pitting potential and wider range of passive potential. Electrochemical impedance spectroscopy (EIS) confirms the formation of a solid passive film on the alloy surface due to a significant increase in the passive film and the charge transfer resistance, as well as lower film and double layer constant phase element magnitude values. Additionally, the potentiostatic polarisation results also show a lower passive current density and passive film stability, resulting in an increase in the breakdown time when the amount of strontium added to the alloy increases from 0.0 to 1.0 wt%. Furthermore, the scanning electron microscopy results indicate that insignificant corrosion is observed on alloy specimens containing strontium, whereas there is fierce corrosion on alloy based surfaces. This robust corrosion resistance could be attributed to the α-grain reduction and refined precipitates at the alloy grain boundaries, resulting in promoted formation of the passive film which is formed from a mixture of magnesium, aluminum and tin oxides/hydroxides, as confirmed by the X-ray photoelectron spectroscopy results.

Received 1st March 2020
Accepted 28th August 2020

DOI: 10.1039/d0ra01956a

rsc.li/rsc-advances

Introduction

Magnesium alloys have shown a continuous increase in annual production and have reached a wide level of applications matching their advantageous properties, such as resistance to heat/creeping, low density, good castability, stiffness, energy absorption, strength and surface quality.[1] Their advantages play an important role in the electronic, automobile and aerospace industries, as well as in bio-applications.[2] Unfortunately, their corrosion resistance is still questionable when magnesium alloys are applied in such industries since the magnesium alloy surface expresses a high chemical reactivity. Therefore, overcoming this weakness of corrosion resistance is a very important and urgent task for developing sturdy alloys. To date, many attempts, such as alloying elements,[3–5] coatings,[6,7] surface treatment,[8,9] rolling and equal-channel angular pressing[10,11] have been tried to overcome this challenge.

Among these technologies for the development of magnesium alloys, alloying elements is one notable way to improve the electrochemical corrosion resistance on account of solid solution strengthening, grain reduction and continuously refined precipitation.[12] The basic elements, including Fe, Cu, Mn, Ni, Al, Ca, Li, Sr, Zn, and Zr, and the rare earth elements (Mm) have been considered for the development of magnesium alloys. It has been indicated that the electrochemical corrosion resistance of magnesium alloys strongly depends on the second phase and microstructure when alloying elements are used.[13–16] For instance, when heavy elements such as Fe, Cu, Mn and Ni are used, an intermetallic phase containing Fe, Cu, Mn and Ni could appear at a minor level, resulting in micro-galvanic corrosion. Therefore, they seem to be an impurity, a deleterious influence on corrosion resistance due to the formation of a micro-galvanic couple and/or hindering the maintenance of a protective layer on the alloy surface.[17,18]

Aluminium (Al) seems to be the most commonly added element to Mg due to its lightness, low cost and improvement in strength.[19,20] Additionally, the anodic kinetics of Mg could be reduced if the amount of Al added to Mg is lower than the solubility limit (about 12 wt%). The addition of Al to Mg can produce a protective film on the alloy surface, with a dense and

[a]*PetroVietnam University, 762 Cach Mang Thang Tam Street, Long Toan Ward, Ba Ria City 790000, Vietnam*

[b]*Chemical Engineering Department, Universiti Teknologi Petronas, Bandar Seri Iskandar 32610, Perak, Malaysia*

[c]*College of Engineering, IT & Environment, Charles Darwin University, 0909, Australia*

[d]*Institute of Research and Development, Duy Tan University, Danang 550000, Vietnam. E-mail: tranvanhung9@duytan.edu.vn; nguyendangnam@duytan.edu.vn*

[e]*The Faculty of Environmental and Chemical Engineering, Duy Tan University, Danang 550000, Vietnam*

[f]*Department Engineering of Petroleum Processing and Environmental Protection, Petroleum-Gas University of Ploiesti, 100680 Ploiesti, Romania. E-mail: cpanaitescu@upg-ploiesti.ro*

compact nature due to passive film formation built up by a mixture of Mg and Al oxides and/or Mg and Al hydroxides on the alloy surface. However, the corrosion resistance of these alloy types is still questionable when 5 wt% Al is added to Mg and the mechanical properties are also influenced by the second phase, $Mg_{17}Al_{12}$, which cannot reach a pinning-grain boundary at the required temperature.[21,22] Therefore, other elements can be considered for addition to the Mg–5Al alloy system to ameliorate the required properties, including corrosion resistance and mechanical properties, to expand the applications of the Mg–5Al alloy. Tin (Sn) could be a good candidate for an alloying element that could be added to the Mg–5Al alloy due to its straightforward interactions and low cost. When Sn is oxidised in aqueous solution, the Sn(IV) product, such as SnO_2, is stable in both acidic and alkaline solutions.[23] Additionally, Sn could significantly increase the anodic activity due to its low exchange current density. Park and colleagues reported that when Sn was added to an Mg alloy, Mg_2Sn could form along grain boundaries with a high volume fraction.[24–27] Furthermore, strontium can form $Mg_{17}Sr_{12}$ along grain boundaries and exhibits low solid solubility when it is added to Mg. When Sr is used as an alloying element for Mg–Al–Zn alloy systems, the α-grain size could be reduced and binary eutectic formation, including Al_4Sr, $Mg_{17}Sr_{12}$ and Mg_2Sr, occurs at the grain boundaries with a homogeneous distribution. These benefits could result in a decrease in the volume fraction of intermetallic $Mg_{17}Al_{12}$.[28–32] The addition of Sr can induce grain refinement, resulting in an increase in the tensile strength of Mg alloys and the promoted formation of the protective film on the alloy surface.[33,34] Also, the addition of Sr can significantly decrease the second phase spacing and increase the $Mg_{17}Sr_2$ fraction, as well as reducing dendrite segregation and micro-galvanic corrosion.[35,36] In particular, Sr has an important role in the bones of the human body as a natural bone-seeking element and it provides biocompatibility, corrosion resistance and good mechanical properties to Mg alloys.[37–40] Therefore, the influence of Sr addition (as an alloying element) on the microstructure and alkaline corrosion resistance of Mg–5Al–4Sn based alloys has been examined using surface analysis and advanced electrochemical techniques in an aggressively saline solution (pH 14).

Methods

The Mg–5Al–4Sn–*x*Sr (*x* is 0.0, 0.5 and 1.0 wt%, respectively) alloys were fabricated by a die casting method with 320-tonne high pressure. The optical emission spectroscopy measurements showed that there were imperceptible differences between the measured and specified compositions of Al, Sn and Sr. Furthermore, the Fe/Mn ratio was about 0.032, suggesting the influence of Fe and Mn concentrations on the corrosion properties of the investigated alloys.[41] The same position on the cast alloys was used for microcutting a specimen with dimensions of 1 cm × 1 cm × 0.3 cm which was used for all surface and electrochemical analyses. To ensure the exposed area was 1 cm^2 in the electrochemical measurements, these fabricated specimens were cool-mounted using a low viscosity epoxy with EpoFix resin and a hardener. X-ray diffraction (XRD) with Cu Kα radiation was undertaken at 0.02° with a step scan from 20 to 80° of 2θ to obtain the phases and alloy microstructures. The working electrodes used for the electrochemical measurements were finished by grinding with 1000-grit silicon carbide (SiC) paper and ethanol was used during the grinding process to avoid oxidation. To characterise the alloy microstructures, the specimens above were ground and finished with #4000 sandpaper. Finally, these ground specimens were then polished with 1 μm alumina powders. The alloy microstructures were characterised using electron probe microanalysis (EPMA) after polishing and scanning electron microscopy/energy dispersive X-ray spectroscopy and after these polished specimens had been etched in 0.008 M HNO_3 solution for 12 seconds.

All electrochemical measurements were carried out in 0.01 M NaCl solution (NaOH was used to adjust the pH to 14 as a passivity study) at room temperature. To remove oxygen from the investigated solution, nitrogen gas was bubbled for 2 h before and during the electrochemical measurements, which were undertaken using a VSP system (BioLogic Scientific Instruments) which is an AC measurement system and uses a commercial software program. The three electrode system, including an alloy specimen as the working electrode and two graphite rods and a saturated calomel electrode (SCE) as the counter and reference electrodes, respectively, was used in a cylindrical electrochemical test cell. Before all electrochemical measurements, the alloy specimens were kept in the solution for 2 h to reach a stable open-circuit potential (OCP). A sinusoidal perturbation of 10 mV for a peak-to-peak amplitude and a 100 kHz to 10 mHz frequency range were used for electrochemical impedance spectroscopy (EIS) measurements. Potentiodynamic measurements were performed at a rate of 0.166 mV s^{-1} and swept in a range between an initial potential of −250 mV_{OCP} and the final potential reached at 10^{-4} mA cm^{-2} during the polarization processes. Furthermore, potentiostatic polarisations were carried out and the anodically applied potential was chosen based on the potentiodynamic polarisation results.

To examine the relationship between the corrosion behaviour and surface morphology, the alloy surface after potentiostatic polarisation was characterised by scanning electron microscopy/energy dispersive X-ray spectroscopy (SEM/EDS). Additionally, the passive film components formed on the alloy surface after 2 h of exposure time at the OCP were characterized using X-ray photoelectron spectroscopy at an anodic voltage of 15 kV and current of 10 mA with an Al Kα energy source.

Results and discussion

Fig. 1 presents the X-ray diffraction patterns of Mg–5Al–4Sn, Mg–5Al–4Sn–0.5Sr and Mg–5Al–4Sn–1.0Sr alloys and shows the main broad peaks as α-Mg, β-$Mg_{17}Al_{12}$ and γ-Mg_2Sn located at the same positions in the results for all specimens. The results also show new, small and sharp peaks obtained in Sr-containing specimens, attributed to the MgAlSr compounds. The intensity of these new, small and sharp peaks increased with increasing Sr content, suggesting that the Sr atoms can occupy and cooperate with Mg and Al in the matrix to form greater amounts of

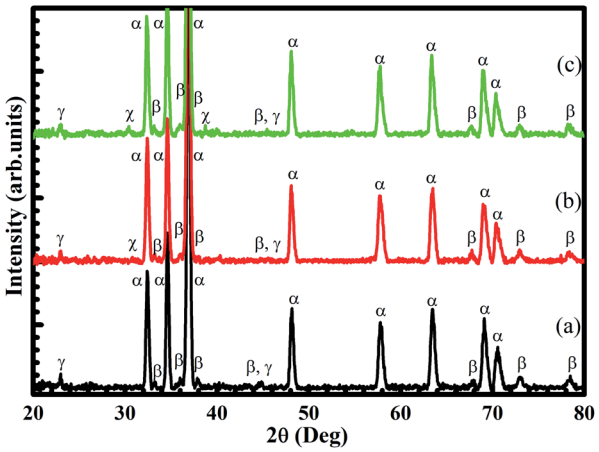

Fig. 1 X-ray diffraction (XRD) results of (a) Mg–5Al–4Sn-based, (b) Mg–5Al–4Sn–0.5Sr and (c) Mg–5Al–4Sn–1.0Sr alloys (α-Mg, β-$Mg_{17}Al_{12}$, γ-Mg_2Sn and χ-MgAlSr).

MgAlSr compounds. This phenomenon could influence both β-$Mg_{17}Al_{12}$ and γ-Mg_2Sn phases, which could be reduced and refined upon themselves. These results can be confirmed *via* SEM after etching and EPMA measurements.

Fig. 2(a–c) compares the SEM results of Mg–5Al–4Sn, Mg–5Al–4Sn–0.5Sr and Mg–5Al–4Sn–1.0Sr alloys after 12 seconds of etching in 0.008 M HNO_3 solution, displaying an obvious α-Mg grain and precipitates of α-Mg, β-$Mg_{17}Al_{12}$, γ-Mg_2Sn and MgAlSr compounds at the grain boundaries. This shows a significant difference between the microstructures of Mg–5Al–4Sn-based specimens and those containing Sr. Relating to the XRD results, the precipitates in the Mg–5Al–4Sn-based alloy microstructure could be assigned to α-Mg, β-$Mg_{17}Al_{12}$ and γ-Mg_2Sn phases. Additionally, a new χ-MgAlSr phase was obtained only in the microstructures of the Sr-containing specimens. Larger α-Mg grain sizes, and sparse and discontinuous precipitates were obtained in the Mg–5Al–4Sn-based alloy microstructure, whereas smaller α-Mg grain sizes, and more dense and continuous precipitates shaped the microstructures of Sr-containing specimens. The precipitates were also characterized *via* energy-dispersive X-ray spectroscopy (EDS, Fig. 2(d and e)) and such combined results suggested that the Mg–5Al–4Sn-based alloy microstructure confirmed that the matrix (black phase) was α-Mg, with the grey and white precipitates being attributed to $Mg_{17}Al_{12}$ and Mg_2Sn. It also suggested that the $Mg_{17}Al_{12}$ phase was mainly located around and was sometimes surrounded by the Mg_2Sn precipitates. For the microstructures of the Sr-containing alloys, Sr was always located at the centre of the precipitates, indicating that MgAlSr compounds could be surrounded by β-$Mg_{17}Al_{12}$ and γ-Mg_2Sn phases, as shown in the EPMA results. These phenomena could result in smaller α-Mg grain sizes, and more dense and continuous precipitates in the microstructures of the Sr-containing alloys.

The elemental distribution of Mg, Al, Sn and Sr in the alloy microstructures was characterised *via* electron probe micro-analysis mapping and the results are given in Fig. 3. It is apparent that greater refinement of the Al and Sn distribution was observed when Sr was added to the base alloy. In particular, Al, Sn and Sr were concentrated at the alloy grain boundaries, confirming the β-$Mg_{17}Al_{12}$, γ-Mg_2Sn and MgAlSr locations in the alloy microstructure. Therefore, the EPMA mapping results are consistent with the XRD and SEM/EDS results. The formation of the new MgAlSr phase could result from a significant reduction in the $Mg_{17}Al_{12}$ phase when Sr was added to the base alloy. Furthermore, γ-Mg_2Sn and MgAlSr precipitates are more stable than $Mg_{17}Al_{12}$, resulting in the microstructural stability and improved corrosion resistance of Mg–5Al–4Sn alloy systems.[42–44] These benefits could create good conditions for the barrier layer to germinate and anchor, developing a compact passive film with a mixture of oxides/hydroxides on the alloy surface, directly affecting the corrosion performance.

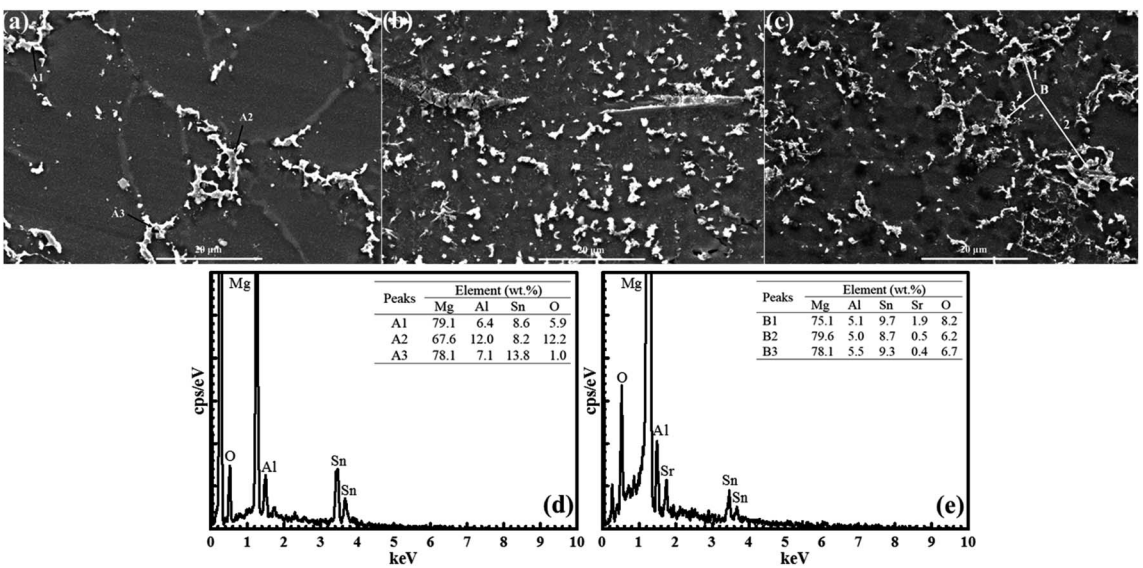

Fig. 2 Scanning electron microscope micrographs of (a) Mg–5Al–4Sn-based, (b) Mg–5Al–4Sn–0.5Sr and (c) Mg–5Al–4Sn–1.0Sr alloys, EDS analysis for intermetallic particles in (d), (a) and (e) (c).

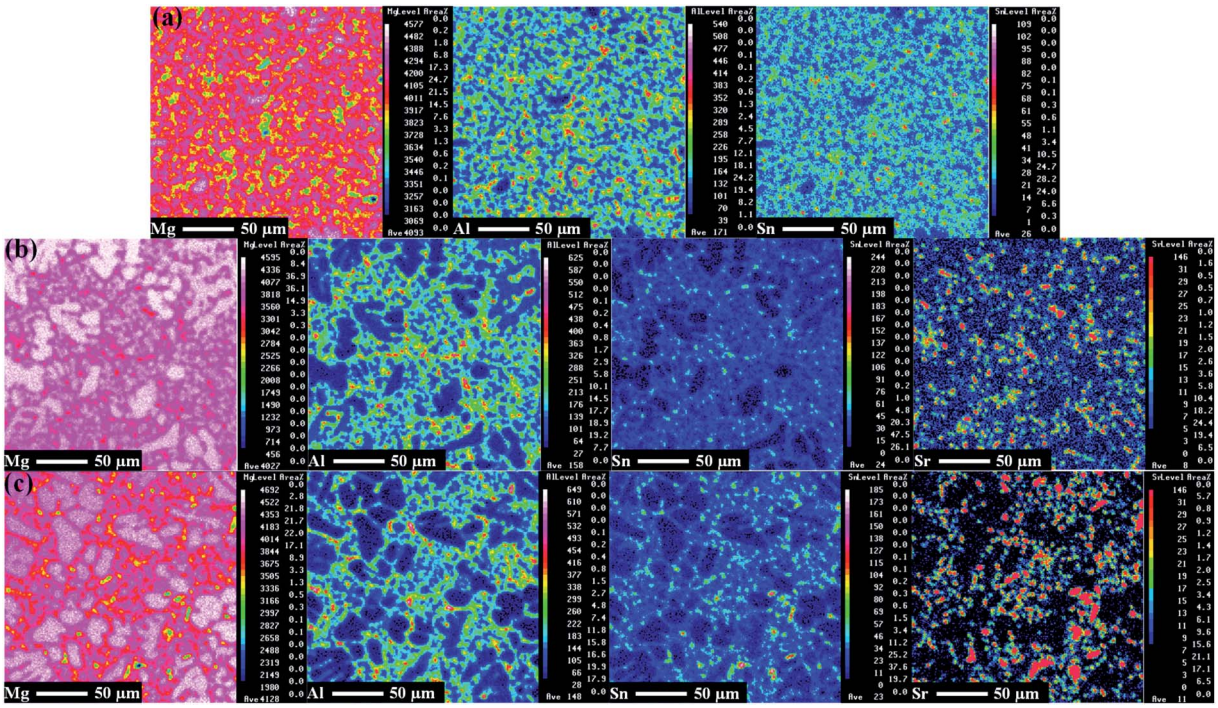

Fig. 3 Electron probe microanalyzer mapping results of chemical elements on the surface of the (a) Mg–5Al–4Sn-based, (b) Mg–5Al–4Sn–0.5Sr and (c) Mg–5Al–4Sn–1.0Sr alloys.

To confirm the above results and assumptions, as well as to characterise the chemical state of Mg, Al, Sn and O in the passive film formed on the alloy surfaces, XPS analysis of the Mg–5Al–4Sn-based and Mg–5Al–4Sn–1.0Sr alloy surfaces was performed after 2 h of exposure in the investigated solution, as shown in Fig. 4. All surveyed spectra results consisted of Mg 2p, Al 2p, Sn 3d and O 1s, ensuring the presence of Mg, Al and Sn products on the alloy surfaces, as shown in Fig. 4(a). Atomic percentages of Mg, Al, Sn and O were 27.276, 3.246, 0.152 and 69.326% for the Mg–5Al–4Sn specimen, while they were 26.045, 3.328, 0.282 and 70.345% for the Mg–5Al–4Sn–1.0Sr specimen. In particular, the KLL Auger line was obtained on both surfaces, suggesting an amount of magnesium metal was present. It also showed that a larger peak was obtained on the Mg–5Al–4Sn-based alloy surface in comparison to that obtained on the Mg–5Al–4Sn–1.0Sr alloy surface, indicating that the addition of Sr had significant influence on the oxidation of Mg. This is also supported by the changes in the corresponding narrow scan spectra of O 1s, as given in Fig. 4(f), which presents a drastic decrease in both the oxide and hydroxide component peaks. A decrease in the Mg KLL Auger line and oxides/hydroxides should contribute to a reduction in the oxidation process observed on the Mg–5Al–4Sn–1.0Sr alloy surface. Fig. 4(b–d) shows the Mg 2p, Al 2p and Sn 3d spectra, which are in accordance with the Mg, Al and Sn oxide/hydroxide products, respectively.[45,46] Lower peak intensities of Mg 2p and Al 2p were observed on the Mg–5Al–4Sn-1.0Sr alloy surface, indicating less dissolution of Mg and Al. However, a significant increase in the peak intensity of Sn 3d was found on the Mg–5Al–4Sn–1.0Sr alloy surface, indicating that addition of Sr directly promoted the Sn contribution on the passive film. Fig. 4(e) indicates that there were no Sr peaks detected on the Mg–5Al–4Sn–1.0Sr alloy surface, suggesting an indirect contribution of Sr into the passive film. Therefore, the XPS results show that the sturdy

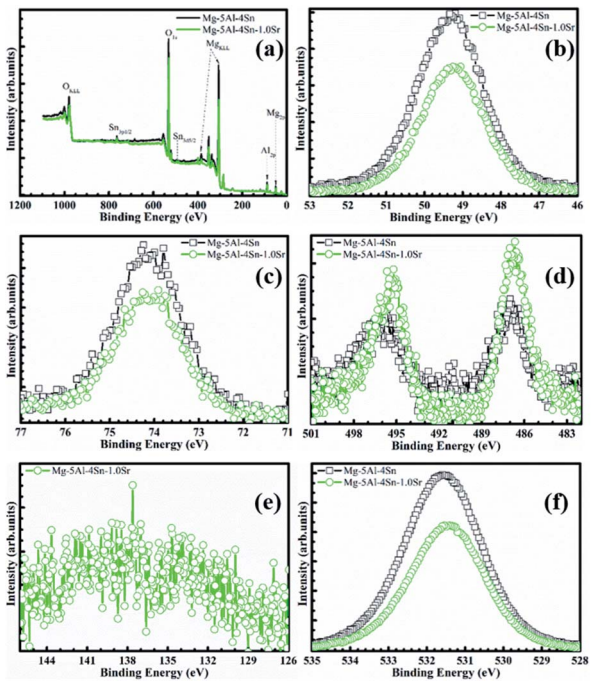

Fig. 4 X-ray photoelectron spectroscopy analysis for the surface components of the Mg–5Al–4Sn-based and Mg–5Al–4Sn–1.0Sr alloys: (a) survey spectra results and (b) Mg, (c) Al, (d) Sn, (e) Sr and (f) O.

passive film formed on the Mg–5Al–4Sn–1.0Sr alloy surface *via* a mixture of oxide/hydroxide alloy components contains mainly Mg, Al and Sn. The enrichment of the incorporated oxides/hydroxides could be attributed to the microstructural benefits, making the passive film more robust for protecting against corrosion, suggesting an important role of alloy microstructures in the formation processes of a sturdy passive film on the magnesium alloy system.

We can now correlate the microstructural properties and passive film component with the electrochemical characterisations. The XRD, SEM/EDS, EPMA mapping and XPS results displayed the important contribution of the alloy microstructures, affected by the addition of Sr in the sturdy passive film formed on the Mg–5Al–4Sn–*x*Sr alloy surfaces, resulting in more robust corrosion resistance. This information was combined with the electrochemical analysis, which represented the presence of a passive film at low current densities as well as higher pitting potentials associated with a larger passive potential range when Sr contents increased up to 1 wt%, as shown in the potentiodynamic polarisation analysis in Fig. 5. Fig. 5(a) indicates that all alloy specimens were well passivated at low current density, related to a high resistance to corrosion. The surface passivation formed on the alloy surfaces could emanate from the presence of a mixture of oxides/hydroxides within the passive film. The good passivation could be related to their different film compositions due to the changes in alloy microstructure *via* Sr addition. Fig. 5(b) shows an extended passivation potential range, with an increase in Sr content that was obviously performed on the anodic branches before the protective oxide films were broken down at the trans-passive area, resulting in pitting at the weak position on the alloy surfaces. The robustness of the solid passive film should result in a higher pitting potential and a lower passive current density, as shown in Fig. 5(a). After the breakdown potential, the current densities should be strongly increased with an increase in the anodic potentials, resulting in an increase in deeper and wider pits, as well as new pit growth. The observed passivation range in the potentiodynamic polarisation results presents a proportional relationship with the Sr added to Mg–5Al–4Sn-based alloy, as shown in Fig. 5(b). The results also showed that the increase in Sr addition tends to be more profitable to the passivation properties on the alloy surfaces. In particular, Sr addition significantly affected oxide film formation and its components, resulting in improved pitting resistance of the Mg–5Al–4Sn–*x*Sr alloy system in the NaCl solution.

To ensure the stability of the performance of the solid passive film in polarisation and XPS results, potentiostatic measurements were carried out at an anodic potential of 800 mV_{SCE}, which corresponded to the breakdown potential of the Mg–5Al–4Sn–0.5Sr alloy specimen and the results are given in Fig. 6. Fig. 6 indicates that an immediate strong increase in current density was observed on the Mg–5Al–4Sn-based alloy specimen, causing breakdown of the passive film when an anodic potential of 800 mV_{SCE} was applied to the working electrode. This suggested that a severe dissolution reaction occurred as $Mg - 2e \rightarrow Mg^{2+}$.[47,48] The current densities then decreased when Sr was added to the alloys and produced a lower value on the Mg–5Al–4Sn–1.0Sr alloy specimen, probably due to the stability of the solid passive film formed on the alloy surface. Easy breakdown of the passive film could contribute to partial precipitation, such as larger α-Mg grain, and sparse and discontinuous precipitates which could be attributed to the existence of greater impurities in comparison with other microstructures. In contrast, smaller α-Mg grains and more

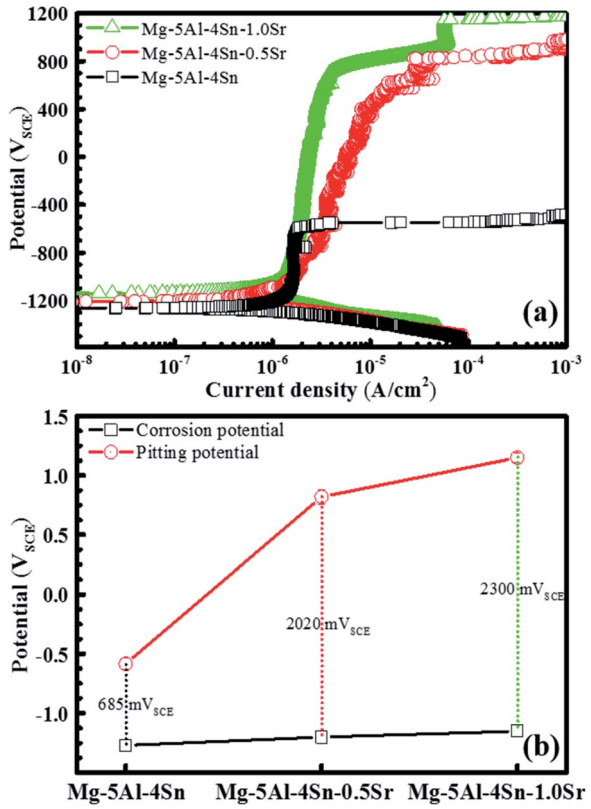

Fig. 5 (a) Potentiodynamic polarization analysis of Mg–5Al–4Sn alloys as a function of Sr content and (b) role of Sr additions in corrosion and pitting potentials as well as a range of passive potentials of the Mg–5Al–4Sn–*x*Sr alloy system.

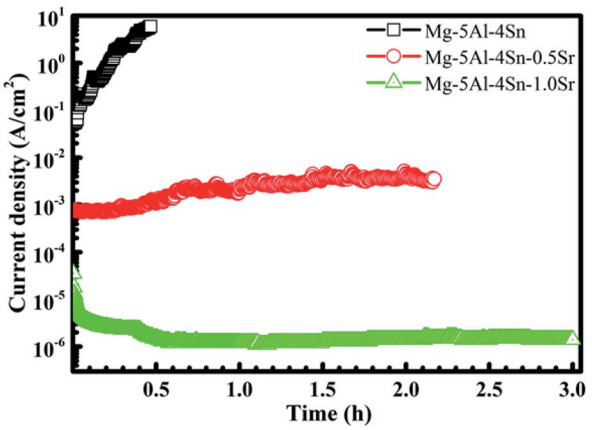

Fig. 6 Changes in current density as a function of time under a constant applied anodic potential of 800 mV_{SCE}.

dense and continuous precipitates in the microstructures of the Sr-containing alloys could promote the formation of the solid passive film, resulting in the significant reduction in anodic current densities observed for the Sr-containing alloy specimens. The very low current density observed in the Mg–5Al–4Sn–1.0Sr alloy specimen could likely be the result of the formation of an oxide/hydroxide mixture, as previously shown in the XPS results. The results again confirmed that addition of Sr could contribute to the passivation properties formed on the alloy surfaces, which should be compact and stable due to the microstructural benefits of the Sr-containing alloys. The above potentiodynamic and potentiostatic polarisation results are in agreement with the SEM results after application of an anodic potential of 800 mV_{SCE}, as presented in Fig. 7. Fig. 7 shows that the surface properties and morphology were strongly influenced by the addition of Sr to the alloy. This demonstrated that severe corrosion was observed over the entire Mg–5Al–4Sn-based alloy surface, as shown in Fig. 7(a), whereas less corrosion was observed on the Mg–5Al–4Sn–1.0Sr alloy surface, as shown in Fig. 7(b). The type of corrosion reflected by the morphologies in this figure is general corrosion that could be a result of the long application time of the strongly anodic potential. However, corrosion should be initiated at a number of surface discontinuities due to the major gaps between α-Mg and precipitates in the Mg–5Al–4Sn-based alloy, resulting in localised corrosion. Localised corrosion is continuously developed in terms of both depth and width under the application of the strongly anodic potential, resulting in the general corrosion observed on the Mg–5Al–4Sn-based alloy surface (Fig. 7(a)), while pits did not occur on the Mg–5Al–4Sn–1.0Sr alloy surface (Fig. 7(b)). These surface properties and morphologies were consistent with the results of the potentiostatic tests.

The influence of the Sr that was added to the Mg–5Al–4Sn-based alloy on the electrochemical impedance was characterised and the results are given in Fig. 8. Fig. 8(a) shows the Nyquist plots of the Mg–5Al–4Sn–*x*Sr alloy system after 2 h of exposure in the investigated solution. All specimens showed a similar response in the impedance spectra with two time constants. The Nyquist plots also showed that the depressed diameter of the semicircle increased with an increase in Sr addition due to formation of the passive film. This indicates that the high- and medium-frequency semicircles are generally associated with local surface defects and the process within the passive film, respectively, while a semicircle curve was obviously performed and covered in the low-frequency spectra, contributing to the process at the alloy surface/passive film interface. The results show that an increase in Sr content increased the semicircle arc, promoting an improvement in the passive film

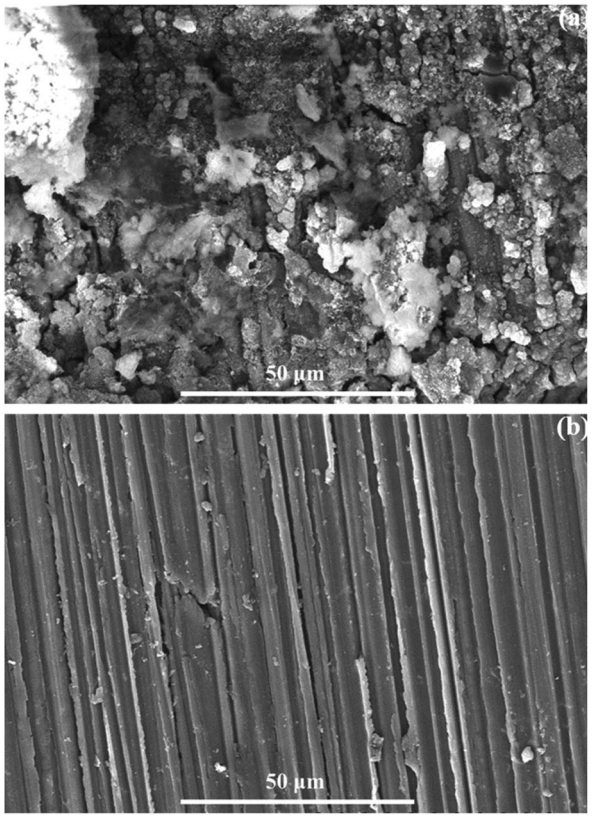

Fig. 7 SEM images of (a) Mg–5Al–4Sn and (b) Mg–5Al–4Sn–1.0Sr alloys after applying a constant anodic potential of 800 mV_{SCE}.

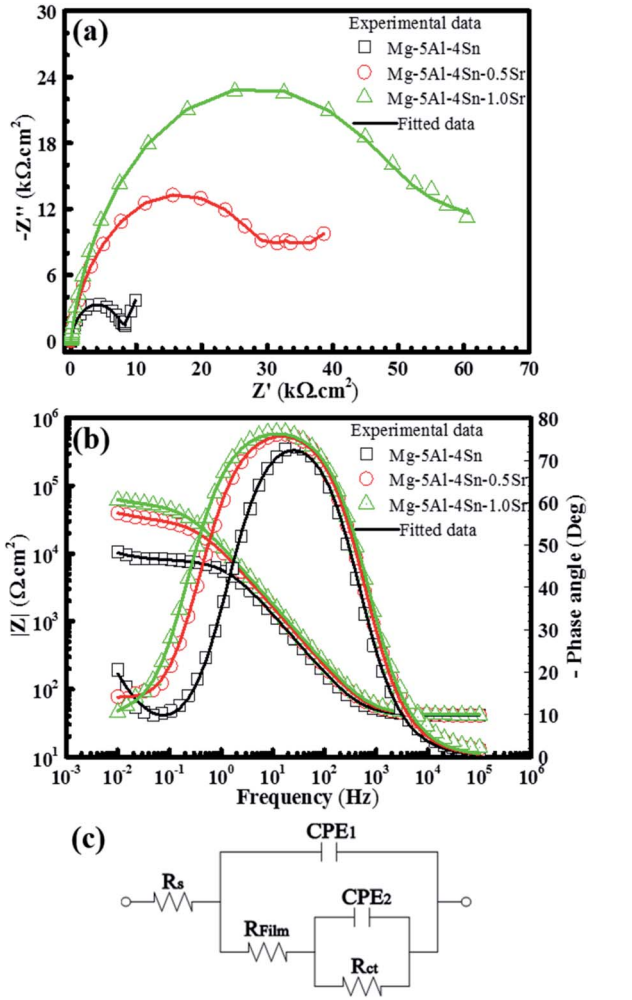

Fig. 8 Impedance spectra of (a) the Nyquist and (b) Bode plots of Mg–5Al–4Sn–*x*Sr alloys and (c) equivalent circuit for fitting EIS data.

resistance and stability. Fig. 8(b) also presents the Bode plots (impedance and phase angle *vs.* frequency) of the impedance spectra. Both the Nyquist and Bode plots present a much larger impedance as well as a higher phase angle for the Sr-containing specimens in comparison with the Mg–5Al–4Sn-based alloy specimen, indicating that the modulus and phase angle are significantly dependent on the addition of Sr. The phase angles also attained a wider range of frequencies when the Sr content increased, as shown in the Bode plots, suggesting a capacitive response. The EIS results clearly showed that a general increase in the overall impedance occurred when Sr was added to the alloy; there was also a slight increase in the high- and medium-frequency impedances. However, a significant increase in the low-frequency impedance was more pronounced with the addition of Sr. A similar trend was also found with the phase angles. These features suggest that the addition of Sr had a profitable effect on the formation of the passive film, resulting in improved corrosion resistance. Based on the microstructure, XPS results and impedance semicircle forms, an equivalent circuit was simulated for fitting the EIS data, given in Fig. 8, where R_s, R_{film}, and R_{ct} are assigned as solution, passive film and charge transfer resistances, respectively. CPE1 and 2 represent the constant phase element of the passive film and double layers. CPE as a symbol of the deviation from an ideal capacitor is used for improving the fitting quality and includes a double-layer capacitance (C) and phenomenological coefficient (n), which can be characterised by $n = 1$, a capacitance; $n = 0.5$, a Warburg impedance; $n = 0$, a resistance and $n = -1$, an inductance.[49,50] In the present study, n was close to 0.7 to 0.9, indicating a deviation from ideal dielectric behaviour.[51–53] Furthermore, the EIS data were fitted by the ZSimpWin program using the equivalent circuit in Fig. 8(c) to optimise the CPE magnitude and resistance parameters and the fitted results are given in Table 1. This indicates that the magnitudes of the passive film and double layer CPE significantly decreased with an increase in Sr content in the Mg–5Al–4Sn-based alloy. Similarly, Table 1 also indicates that higher values of passive film and charge transfer resistances were acquired when increasing the amount of Sr in the Mg–5Al–4Sn-based alloy. These features could result in superior pitting resistance of the Mg–5Al–4Sn–*x*Sr alloy system in the investigated solution.

The three Mg–5Al–4Sn, Mg–5Al–4Sn–0.5Sr and Mg–5Al–4Sn–1.0Sr magnesium alloys have been successfully fabricated and characterised. XRD, SEM/EDS and EPMA mapping results indicated that the significant changes in the microstructure were attributed to the α-Mg grain size reduction, higher density and more continuous precipitates along the grain boundaries that should be caused by Sr addition. In particular, α-Mg grain sizes decreased, and density and continuous precipitates increased with an increase in Sr content, as shown in Fig. 1–3, resulting in more solidity of the alloy microstructures. These benefits could be expected to help easily form a barrier layer on the alloy surfaces. In particular, a more uniform contribution of elements in the alloy microstructure when increasing the Sr content (Fig. 3) could also produce a mixture of oxides/hydroxides for the formation of a solid passive film on the alloy surfaces. Correlatively, XPS measurement indicated that the sturdy passive film was formed on Sr-containing alloy surfaces with a mixture of oxides/hydroxides from the enriched alloy components, including mainly Mg, Al and Sn products, suggesting an improved corrosion resistance.[54–56] Potentiodynamic and potentiostatic polarisation results indicated that the pitting potential, passive potential range and passive stability increased with an increase in the addition of Sr, contributing to the smaller α-Mg grain size, higher density and more continuous precipitates along the grain boundaries, as well as the uniform contribution of alloy elements to the microstructure. As shown in the microstructure analysis, the larger α-Mg grain sizes and sparse and discontinuous precipitates observed on the Mg–5Al–4Sn-based alloy could cause some major gaps between α-Mg and the precipitates, building up the micro-galvanic cells that could create good conditions for corrosion initiation and easily develop to force Mg dissolution later on. This resulted in a lower pitting resistance of the Mg–5Al–4Sn-based alloy, as shown in the electrochemical results. By contrast, the higher pitting resistance and passivation stability observed for the Sr-containing specimens could be attributed to the smaller α-Mg grain size, higher density and more continuous precipitates at the grain boundaries. These benefits could block the defects and gaps between α-Mg and precipitates, inhibiting anodic dissolution and resulting in a delay in pitting initiation. Therefore, the increased pitting potential, passive potential range and passive stability, as well as the resistance and CPE magnitude parameters, should be attributed to the different contributions of the surfaces qualities and compositions found from the XPS results, as well as the alloy microstructures. The smaller α-Mg grain size, higher density and more continuous precipitates at the grain boundaries, as well as the uniform element distribution in the alloy microstructure, help the barrier layer to become more dense and compact *via*

Table 1 Electrochemical impedance spectroscopy (EIS) fitted parameters of Mg–5Al–4Sn–*x*Sr alloys after 2 h of exposure in the 0.01 M NaCl solution (pH 14)

		CPE1			CPE2		
Specimens	R_s (Ω cm^2)	Magnitude (Ω^{-1} cm^{-2} s^n)	n (0–1)	R_{film} (Ω cm^2)	Magnitude (Ω^{-1} cm^{-2} s^n)	n (0–1)	R_{ct} (Ω cm^2)
Mg–5Al–4Sn	41.2	1.91×10^{-5}	0.8834	7960 ± 317	203×10^{-5}	0.6919	9566 ± 260
Mg–5Al–4Sn–0.5Sr	41.9	1.57×10^{-5}	0.8868	16 110 ± 276	94×10^{-5}	0.7513	45 220 ± 483
Mg–5Al–4Sn–1.0Sr	42.1	1.43×10^{-5}	0.8920	20 780 ± 610	55×10^{-5}	0.7937	54 630 ± 270

the incorporation of oxides/hydroxides formed on the Sr-containing alloy surfaces. As shown in the XPS results given in Fig. 4, when the addition of Sr to the alloy increased, the incorporation of oxides/hydroxides increased significantly through the contribution of Mg, Al and Sn products. A denser and more compact passive film being formed on the Sr-containing alloy surface could be strongly dependent on Sr and effectively hinder Cl^- ions penetrating into the alloy surface. It could be concluded that the use of Sr as an alloying element for Mg–5Al–4Sn-based alloys can result in many benefits in terms of α-Mg grain size reduction, higher density, more continuous precipitates and uniform element distributions over the Mg matrix. These act as a barrier layer to enhance dissolution of the Mg–5Al–4Sn-based alloy, resulting in improved corrosion resistance. In particular, these benefits could improve the interaction of Mg, Al and Sn oxides/hydroxides to form a solid and stable passive film on the alloy surfaces.

Conclusions

Mg–5Al–4Sn–*x*Sr alloys where the Sr content ranged from 0.0 to 1.0 wt% were fabricated to consider the effects of Sr content on the microstructures and alkaline corrosion resistance of the Mg–5Al–4Sn-based alloy in a systematic manner. Sr addition reduced the α-grain and refined precipitates at the alloy grain boundaries where a rich and homogeneous Sr distribution was obtained. Also, Sr addition could promote more continuous $Mg_{17}Al_{12}$ and Mg_2Sn precipitation at the grain boundaries *via* some added $Mg_{17}Sr_{12}$, Al_4Sr and AlSr compounds. Electrochemical measurements indicated that the Mg–5Al–4Sn-based alloy became much more sturdy against pitting resistance due to an increase in the pitting potential, passive potential range, passive stability and film and charge transfer resistances, as well as a reduction in the film and double layer's constant phase element magnitude values when the amount of Sr added to the Mg–5Al–4Sn-based alloy increased from 0.0 to 1.0 wt%. Surface analysis showed that significant corrosion was obtained on the surface of Mg–5Al–4Sn-based alloys, while there was less corrosion with the Sr-containing alloys. XPS measurements confirmed that the compact passive film formed on Mg–5Al–4Sn–*x*Sr alloy surfaces was composed of a mixture of Mg, Al and Sn oxides/hydroxides that mainly contain Mg and Al oxides/hydroxides. Furthermore, the Mg, Al and Sn oxides/hydroxides were more abundant when the amount of Sr added to the alloy increased. These benefits, including α-grain reduction, continuous refined precipitates and homogeneous distribution of Sr addition, resulted in the formation of a solid passive film on the Mg–5Al–4Sn–*x*Sr alloy surface. This could hinder the aggressive ion penetration into the investigated alloy surface, resulting in a robust alloy with higher localised corrosion resistance.

Conflicts of interest

The authors declare that they have no known competing financial interests or personal relationships that could have appeared to influence the work reported in this paper.

Acknowledgements

This work is funded by PetroVietnam University under grant code GV1911.

Notes and references

1 V. V. Joshi, J. B. Jordon, D. Orlov and N. R. Neelameggham, *Magnesium Technology 2019*, Springer International Publishing, 2019.
2 B. Viehweger, A. Karabet, M. During and L. Schaeffer, *Materialwiss. Werkstofftech.*, 2005, **36**, 211.
3 N. D. Nam, *J. Electrochem. Soc.*, 2016, **163**, C76.
4 N. D. Nam, *J. Magnesium Alloys*, 2014, **2**, 190.
5 M. Z. Bian, A. Tripathi, H. Yu and L. M. Yan, *Mater. Sci. Eng., A*, 2015, **639**, 320.
6 M. B. Kannan, R. Walter, A. Yamamoto, H. Khakbaza and C. Blawert, *RSC Adv.*, 2018, **8**, 29189.
7 Y. Li, S. Cai, G. Xu, S. Shen, M. Zhang, T. Zhang and X. Sun, *RSC Adv.*, 2015, **5**, 25708.
8 G. Zhang, L. Wu, A. Tang, B. Weng, A. Atrens, S. Ma, L. Liu and F. Pan, *RSC Adv.*, 2018, **8**, 2248.
9 N. Palaniappan, I. S. Cole, A. E. Kuznetsov, K. Balasubramanian and K. R. Justin Thomas, *RSC Adv.*, 2019, **9**, 32441.
10 J. H. Lee, S. W. Lee and S. H. Park, *J. Mater. Res. Technol.*, 2019, **8**, 3167.
11 H. Huang, H. Liu, C. Wang, J. Sun, J. Bai, F. Xue, J. Jiang and A. Ma, *J. Magnesium Alloys*, 2019, **7**, 617.
12 G. L. Song, *Corrosion of Magnesium Alloys*, Woodhead Publishing, 1st edn, 2011.
13 M. Z. Bian, X. Huang and Y. Chino, *J. Alloys Compd.*, 2020, **837**, 155551.
14 M. Z. Bian, X. Huang, M. Mabuchi and Y. Chino, *J. Alloys Compd.*, 2020, **818**, 152891.
15 J. Bohlen, S. Meyer, B. Wiese, B. J. C. L. Feyerabend, R. W. Römer and D. Letzig, *Materials*, 2020, **13**, 391.
16 N. D. Nam, J. G. Kim, K. S. Shin and H. C. Jung, *Scr. Mater.*, 2010, **63**, 625.
17 H. Krawiec, S. Stanek, V. Vignal, J. Lelito and J. S. Suchy, *Corros. Sci.*, 2011, **53**, 3108.
18 S. Yao, S. Liu, G. Zeng, X. Li, T. Lei, Y. Li and Y. Du, *Metals*, 2019, **9**, 460.
19 K. U. Kainer, P. Bala Srinivasan, C. Blawert and W. Dietzel, *Shreir's Corrosion*, 2010, vol. 3, p. 2011.
20 M. Gupta and N. M. L. Sharon, *Magnesium, Magnesium Alloys and Magnesium Composites*, John Wiley & Sons, Hoboken, 2011.
21 M. G. Jiang, C. Xu, T. Nakata, H. Yan, R. S. Chen and S. Kamado, *J. Alloys Compd.*, 2016, **668**, 13.
22 S. H. Kim, S. W. Lee, B. G. Moon, H. S. Kim, Y. M. Kim and S. H. Park, *J. Mater. Res. Technol.*, 2019, **8**, 5254.
23 A. J. Bard, R. Parsons and J. Jordan, *Standard potentials in aqueous solution*, Marcel Dekker Inc., New York, 1985.
24 K. C. Park, B. H. Kim, H. Kimura, Y. H. Park and I. M. Park, *Mater. Trans.*, 2010, **51**, 472.

25 B. H. Kim, K. C. Park, Y. H. Park and I. M. Park, *Trans. Nonferrous Met. Soc. China*, 2010, **20**, 1184.
26 K. C. Park, B. H. Kim, H. Kimura, Y. H. Park and I. M. Park, *Mater. Trans.*, 2012, **53**, 362.
27 S. G. Lee, J. J. Jeon, K. C. Park, Y. H. Park and I. M. Park, *Mater. Sci. Eng., A*, 2011, **528**, 5394.
28 M. Zhou, X. Huang, Y. Morisada, H. Fujii and Y. Chino, *Mater. Sci. Eng., A*, 2020, **769**, 138474.
29 N. D. Nam, W. C. Kim, J. G. Kim, K. S. Shin and H. C. Jung, *J. Alloys Compd.*, 2011, **509**, 4839.
30 Y. Zhang, L. Yang, J. Dai, J. Ge, G. Guo and Z. Liu, *Mater. Sci. Eng., A*, 2014, **610**, 309.
31 M. Celikin, A. A. Kaya and M. O. Pekguleryuz, *Mater. Sci. Eng., A*, 2012, **550**, 39.
32 M. Celikin and M. O. Pekguleryuz, *Mater. Sci. Eng., A*, 2012, **556**, 911.
33 M. Cheng, J. Chen, H. Yan, B. Su, Z. Yu, W. Xia and X. Gong, *J. Alloys Compd.*, 2017, **691**, 95.
34 T. Ding, H. G. Yan, J. H. Chen, W. J. Xia, B. Su and Z. L. Yu, *Trans. Nonferrous Met. Soc. China*, 2019, **29**, 1631.
35 A. Sadeghi, E. Hasanpur, A. Bahmani and K. S. Shin, *Corros. Sci.*, 2018, **141**, 117.
36 Y. Fu, H. Wang, C. Zhang and H. Hao, *Mater. Sci. Eng., A*, 2018, **723**, 118.
37 H. Pan, K. Pang, F. Cui, F. Ge, C. Man, X. Wang and Z. Cui, *Corros. Sci.*, 2019, **157**, 420.
38 J. Wang, Y. Ma, S. Guo, W. Jiang and Q. Liu, *Mater. Des.*, 2018, **153**, 308.
39 X. Meng, Z. Jiang, S. Zhu and S. Guan, *J. Alloys Compd.*, 2020, **838**, 155611.
40 Z. Gao, M. Song, R. L. Liu, Y. Shen, L. Ward, I. Cole, X. B. Chen and X. Liu, *Mater. Sci. Eng., C*, 2019, **104**, 109926.
41 G. L. Makar and J. Kruger, *Int. Mater. Rev.*, 1993, **38**, 138.
42 L. Li and N. D. Nam, *J. Magnesium Alloys*, 2016, **4**, 44.
43 B. X. Vuong, N. S. H. Vu, T. D. Manh, M. Vaka, D. X. Du and N. D. Nam, *Mater. Lett.*, 2018, **228**, 309.
44 K. H. Kim, N. D. Nam, J. G. Kim, K. S. Shin and H. C. Jung, *Intermetallics*, 2011, **19**, 1831.
45 J. F. Moulder, W. F. Stickle, P. E. Sobol and K. D. Bomben, *Handbook of X-ray photoelectron spectroscopy*, Perkin-Elmer Corp, Eden Prairie, MN, USA, 1992.
46 N. D. Nam, W. C. Kim, J. G. Kim, K. S. Shin and H. C. Jung, *Corros. Sci.*, 2009, **51**, 2942.
47 S. N. Potapov, I. A. Gvozdkov, V. A. Belyaev, V. N. Verbetsky and S. V. Mitrokhin, *Int. J. Hydrogen Energy*, 2019, **44**, 28578.
48 M. Uda, H. Okuyama, T. S. Suzuki and Y. Sakka, *Sci. Technol. Adv. Mater.*, 2012, **13**, 025009.
49 J. R. MacDonald, *Impedance Spectroscopy*, Wiley, New York, 1987.
50 J. Solé, L. Bausa and D. Jaque, *An Introduction to the Optical Spectroscopy of Inorganic Solids*, John Wiley & Sons, Inc, 2005.
51 R. Schweiss, C. Werner and W. Knoll, *J. Electroanal. Chem.*, 2003, **540**, 145.
52 E. Barsoukov and J. R. Macdonald, *Impedance Spectroscopy: Theory, Experiment, and Applications*, 2nd edn, John Wiley & Sons, Inc, 2005.
53 J. Wang, *Analytical Electrochemistry*, 3rd edn, John Wiley & Sons, Inc, 2006.
54 B. X. Vuong, H. T. Anh, N. T. Nhan, H. H. M. Xuan, D. C. Nguyen and N. D. Nam, *J. Mater. Eng. Perform.*, 2017, **26**, 3676.
55 R. S. Campos, D. Höche, C. Blawert and K. U. Kainer, in *Influence of Lanthanum concentration on the Corrosion Behaviour of Binary Mg-La Alloys, Magnesium Technology 2011*, ed W. H. Sillekens, S. R. Agnew, N. R. Neelameggham and S. N. Mathaudhu, Springer, Cham, 2011.
56 J. Ding, X. Liu, Y. Wang, W. Huang, B. Wang, S. Wei, X. Xia, Y. Liang, X. Chen, F. Pan and B. Xu, *Materials*, 2019, **12**, 2069.